Check for updates

4040 Vol. 47, No. 16 / 15 August 2022 / Optics Letters Letter

Optics Letters

Visible and near-infrared dual band switchable metasurface edge imaging

GUANGHAO CHEN,[1,†] JUNXIAO ZHOU,[1,†] STEVEN EDWARD BOPP,[2] JUNXIANG ZHAO,[1] AND ZHAOWEI LIU[1,2,*]

[1] Department of Electrical and Computer Engineering, University of California, San Diego, La Jolla, California 92093, USA
[2] Materials Science and Engineering Program, University of California, San Diego, La Jolla, California 92093, USA
*Corresponding author: z4liu@eng.ucsd.edu
† These authors contributed equally to this work

Received 26 May 2022; revised 13 July 2022; accepted 18 July 2022; posted 20 July 2022; published 4 August 2022

Optical edge detection at the visible and near infrared (VNIR) wavelengths is deployed widely in many areas. Here we demonstrate numerically transmissive VNIR dual band edge imaging with a switchable metasurface. Tunability is enabled by using a low-loss and reversible phase-change material Sb_2S_3. The metasurface acts simultaneously as a high-pass spatial filter and a tunable spectral filter, giving the system the freedom to switch between two functions. In Function 1 with amorphous Sb_2S_3, this metasurface operates in the edge detection mode near 575 nm and blocks near infrared (NIR) transmission. In Function 2 with crystalline Sb_2S_3, the device images edges near 825 nm and blocks visible light images. The switchable Sb_2S_3 metasurfaces allow low cross talk edge imaging of a target without complicated optomechanics. © 2022 Optica Publishing Group

https://doi.org/10.1364/OL.465128

As the implementation of multispectral imaging has been growing in sectors like autonomous driving and manufacturing, so too has a need for materials and devices capable of strongly interacting with light over a variety of bandwidths in small form factors. Visible and near infrared multispectral imaging systems [1] combine the benefits of near infrared and visible wavelengths underpinning many dual-band imaging systems. Optical edge imaging extracts morphological information of objects and is broadly applicable in image processing, computation, and machine vision to distinguish objects with enhanced clarity [2]. Spatial filtering at the Fourier plane of an imaging system with traditional elements [3–6] can be used to realize all-optical edge imaging; however, the unwieldy bulk of conventional free space optics hinders miniaturization [7]. Ultrathin optical metasurfaces composed of two-dimensional (2D) electromagnetic structured arrays [8–11] have become widespread for subminiature and chip-integrated optics [12,13] and edge-detectors [14–21].

Even with low-loss dielectrics allowing high VNIR device efficiencies [22–24], costly fabrication and lack of post-fabrication tunability have historically limited the available multiplexing methods on metasurfaces. Recent efforts in creating reconfigurable metasurfaces are expanding the applicability space and easing fabrication for multifunctional metasurfaces [25–29]. Even though tunable metasurfaces have been demonstrated using a variety of means including direct thermal [30], mechanical [31], and electrical [32], as well as with the injection of carriers [33] and exploitation of the Kerr nonlinearity [34], they are frequently a combination of slow, lossy, and limited in their range of tunability [35].

Phase change materials (PCMs) are showing promise as a means of applying post-fabrication tunability to metasurface. PCMs can display large refractive index contrasts across wide operating bandwidths before and after a phase transformation [36,37]. One such PCM of interest in the VNIR range is Sb_2S_3 which can have a larger bandgap and lower absorption [38–40] compared to other PCMs like Ge-Sb-Te (GST) alloys [41–43]. Given this convenience, in this Letter, we present a numerical design of an Sb_2S_3 switchable metasurface for dual-band edge imaging at wavelengths of 575 nm and 825 nm. The switchable functions are multiplexed temporally on a single metasurface.

Figure 1(a) shows the wavelength-dependent refractive indices of amorphous Sb_2S_3 (a-Sb_2S_3) and crystalline Sb_2S_3 (c-Sb_2S_3) [41]. The large and reversible change of the real refractive index is the key to the device switchable capability. The designed dual band metasurface has two roles in the edge imaging system: (1) a point spread function modulator that only transmits high spatial frequencies of the signal and (2) a switchable bandpass filter for 575 nm and 825 nm. Hence, when inserted in a $4f$ system, in Function 1 with a-Sb_2S_3, the device only transmits 575-nm band edge images, blocking other wavelengths, as shown in Fig. 1(b); in Function 2 with c-Sb_2S_3, it transmits 825-nm band edge images instead, as shown in Fig. 1(c).

To realize the switching, two arrays of Sb_2S_3 nanoblocks are interleaved on a fused silica substrate ($n = 1.45$) as shown in Figs. 1(b) and 1(c). The transformation of Sb_2S_3 can be achieved with optimized heating strategies [44]. Each array generates an individually optimized phase profile: one for a-Sb_2S_3 and the other for c-Sb_2S_3. The first array A1 [shown in blue in both Figs. 1(b) and 1(c)] is optimized for Function 1. It shapes the incoming waves into the designed wavefront at a-Sb_2S_3. However, A2 (red) is optimized for Function 2 at c-Sb_2S_3. Thus, when the nanoblocks are a-Sb_2S_3, the device operates at 575 nm. When the nanoblocks are c-Sb_2S_3, the system works

0146-9592/22/164040-04 Journal © 2022 Optica Publishing Group

Corrected 8 August 2022

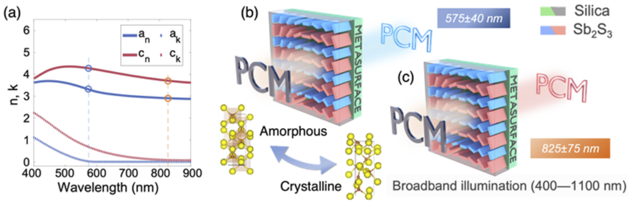

Fig. 1. (a) Wavelength-dependent refractive indices of a-Sb_2S_3 (blue) and c-Sb_2S_3 (red). (b) Function 1 of the metasurface with a-Sb_2S_3 and 575-nm edge image transmission only. (c) Function 2 with c-Sb_2S_3 and 825-nm transmission only. Two Sb_2S_3 arrays, colored in red and blue, interleaved and fully submerged in a fused silica slab. The fused silica covering the arrays is shown as transparent instead of green only to show the details.

at 825 nm. Because of the interleaving of these two structures and the reliance that their properties have on their individual phases, there is little to no overlap of images between the functions. This application of PCMs allows for a non-mechanical switching of metasurfaces and thereby sidesteps many problems relating to the failure of components inherent to systems reliant on mechanical motion.

In either function, the nanostructure array is a phase element for the corresponding spectral band. A geometric phase delay in the transmission arises from the form birefringence created by nanostructures [45]. The local region centered around each metasurface unit cell can be regarded as a rotated anisotropic medium. The wave polarization can be traced with Jones calculus [7] using the complex transmission coefficients t_0 and t_e for the two orthogonal linear polarizations of the geometrical phase metasurface. When described in a helical basis, for the sake of convenience, the field exiting the metasurface is [46]

$$\boldsymbol{E}_{\mathbf{T}} = \frac{\boldsymbol{t}_0 + \boldsymbol{t}_e}{2} \mathrm{E}_{\mathbf{I}}^{\mathbf{R/L}} + \frac{\boldsymbol{t}_0 - \boldsymbol{t}_e}{2} \exp(\boldsymbol{i}\boldsymbol{m}2\boldsymbol{\theta}) \mathrm{E}_{I}^{\mathbf{L/R}}, \tag{1}$$

where E is the electric field, subscripts I and T indicate incident and transmitted field, respectively, superscripts L and R indicate the circular polarization state of the electric field, and m is "−" for right- and "+" for left-handed circularly polarized (RCP and LCP, respectively) light. Equation (1) shows that the field departing the metasurface is the sum of an attenuated zeroth-order field $\mathrm{E}_I^{R/L}$ (incident beam) and a phase-delayed field $\mathrm{E}_I^{L/R}$ with the opposite circular polarization. In the lossless transmission case where $|t_0| = |t_e| = 1$ and $t_0 = t_e \exp(i\pi)$, the zeroth-order term vanishes, while the efficiency of polarization conversion reaches the maximum. Here, θ is the in-plane orientation angle of the nanostructure. The delayed phase, $m2\theta$, of the cross-polarization is linearly proportional to θ and is independent of the wavelength, which contrasts with plasmonic and dielectric resonance phase modulation mechanisms [45,47]. As the birefringent nanostructure rotates from 0° to 180°, the phase of the forward scattered wave changes linearly from 0 to 2π.

We chose rectangular dielectric waveguide meta-atoms, as shown in Fig. 2(a), to create a geometric phase metasurface. Due to the two-fold rotational symmetry of the waveguide cross section, defined by the length (L), width (W), and height (H) in Fig. 2(a), modes excited by the two orthogonal polarizations experience different dispersion in the structure [47]. The cross section of the waveguide is tuned such that t_0 and t_e are 180° out-of-phase in the working wavebands. Hence, the designed phase profile (wrapped to 0–2π) is translated to a θ profile ranging

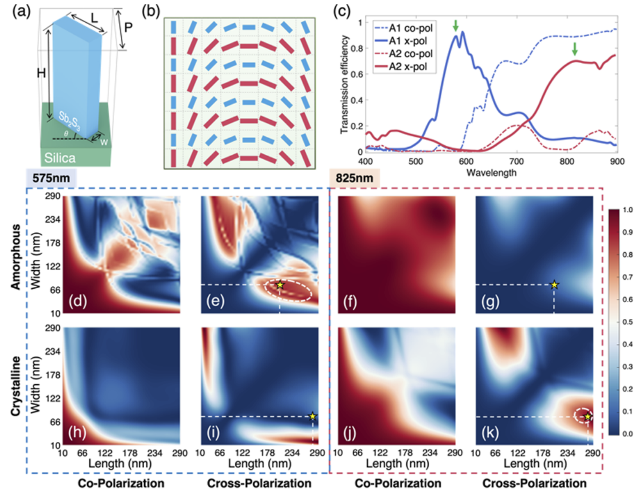

Fig. 2. (a) A unit cell with a Sb_2S_3 nanobar fully embedded in the silica slab. The top silica cover is transparent for the same purpose as in Figs. 1(b), 1(c). (b) A1 (blue) and A2 (red) array interleaved on the substrate. (c) Co-polarization (co-pol) and cross-polarization (cross-pol) transmittance of the unit cells in A1 and A2. (d)–(k) Simulated transmittances in Function 1 or Function 2. These results share the same coordinate and color scale. Dashed ellipses mark the optimal geometries. The stars mark the chosen geometry for each function. The chosen nanoblock cross section is 200 nm × 75 nm for Function 1 and 280 nm × 75 nm for Function 2.

from 0–180° on the metasurface. The commercial finite-element method software COMSOL is used in the nanopillar design. The periodic boundary condition is applied to four sides of the unit cell, and the PML condition is applied to the top and bottom of the simulation domain. The transmittance and phase of the forward scattering coefficient are monitored. By sweeping the geometrical parameters, we identified an optimized shape for Function 1 where high polarization conversion efficiency occurs at the 575-nm band with a-Sb_2S_3 and low efficiency at 825 nm, indicated by the dotted lines in Figs. 2(e) and 2(g). We similarly design for Function 2 with crystalline Sb_2S_3, as shown by the dotted lines in Figs. 2(h)–2(k). Both arrays have the same height H = 500 nm and unit cell period P = 300 nm, which are compatible with the state-of-the-art fabrication processes [47,48]. The Sb_2S_3 structures are fully submerged in fused silica. The latter can prevent oxidation of the chalcogenide material, as well as deformation after many cycles of phase changing [36,44]. Since the functions of arrays A1 and A2 are multiplexed not only spatially but also temporally (that is, only one may be activated at a certain time because of the necessity for phase conversion between operating modes), the cross talk between the two bands is minimized, as evidenced by the well-separated peaks in the polarization conversion efficiency curves shown in Fig. 2(c).

In our system, edge detection is enabled by optical transfer function modulation of a linear polarization (LP) input at the Fourier plane of a $4f$ optical system [14]. The complex transmission function of the metasurface is $T(f_x, f_y) = \exp(im2\pi f_x/\Lambda)$, where $f_x = x'/\lambda f$ and $f_y = y'/\lambda f$. Here, x' and y' are the real space coordinates at the Fourier plane, f is the focal length of the lenses, Λ is the period of the grating, and $2\pi/\Lambda$ is the phase gradient. In the case of a linear polarization input, represented in a helical basis, each circular component is polarization converted, i.e., RCP converted to LCP and vice versa, as well as space shifted

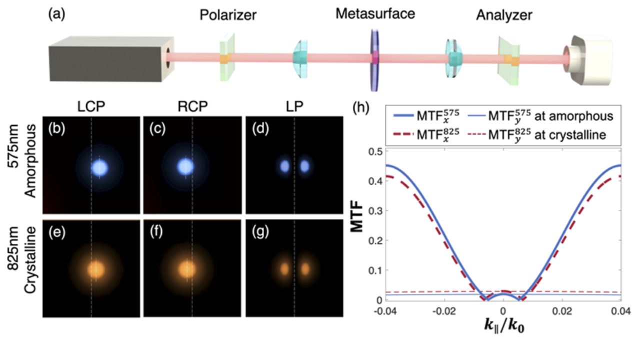

Fig. 3. (a) A $4f$ configuration used in the simulation. Point imaging simulation of (b),(c) LCP or (e),(f) RCP input. In both cases, LCP and RCP outputs are shifted symmetrically to either side of the field. (d) and (g) An LP input splits horizontally into two lobes. (h) System MTFs for the two functions at orthogonal cross sections.

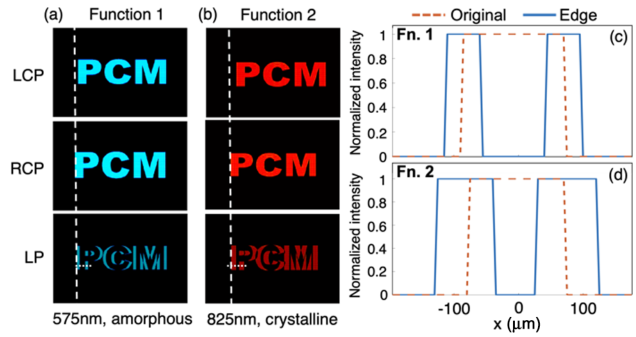

Fig. 4. (a) First two images: simulated imaging results of LCP and RCP in Function 1 (Fn. 1). Third image: detected edge of an LP input. (c) Cross sections of the original and the edge image in panel (a). (b) Similar results in Function 2 (Fn. 2). (d) Cross sections of the original image and the edge image in panel (b). Intensities in both panels (c) and (d) are normalized for better comparison.

along the x axis in one direction. The total distance between the two components is $2\Delta = 2\lambda f/\Lambda$, as indicated in Ref. [14].

The overlapping region of the RCP and LCP field still possesses the same linear polarization as the incident field and is blocked by an analyzer (polarizer) in front of the detector. In the non-overlapping region, as in the case of image edges, the field remains circularly polarized and can reach the CCD (intensity is attenuated by the analyzer). As Δ approaches infinitesimal, the edge-enhanced output can be regarded as a spatial differentiation operation of the input field along the x-direction, i.e., $\mathbf{E}_o(x, y) \cong 2\partial \mathbf{E}_I(x, y)/\partial x$, where $\mathbf{E}_I$ is an LP input and $\mathbf{E}_o$ is the output with orthogonal polarization. This is edge detection like the one-dimensional Sobel operator in digital image processing, except that the method presented here is fully optical and wave band-selective simultaneously.

To aid better understanding, we visualize the functions by simulating field propagation of a Gaussian beam through a $4f$ system, as shown in Fig. 3(a). For either wavelength passing through the system, the Gaussian profile of a circularly polarized beam is unchanged except for being laterally displaced from the center of the image plane arising from the linear phase on the metasurface. The images shift to the right side of the image plane for the LCP field and to the left side for the RCP field, as shown in Figs. 3(b), 3(c) and Figs. 3(e), 3(f). In the case of an LP input with both LCP and RCP components, the overlapped region of the LCP and RCP image is blocked by the analyzer, leaving only edges on the detector, as shown in Figs. 3(d) and 3(g). The modulation transfer functions (MTF) in Figs 3(h) indicate the system is an astigmatic high-pass spatial filter for both functions. Signals with smaller k_x are gradually and selectively suppressed. The magnitudes are reduced due to the presence of a pair of crossed polarizers.

However, for Function 1 or Function 2, the transmittance of wavelengths beyond the working wave band drops dramatically, due to insufficient polarization conversion efficiency of the metasurface.

Edge detection of a more complicated object, boldface letters PCM, is shown in Fig. 4. Like the results in Fig. 3, an LP input [third row in Fig. 4(a) and 4(b)], the overlapped region of the LCP and RCP components is blocked by the analyzer.

The detected edge resolution is the same as the shearing distance, $2\Delta = 2\lambda f/\Lambda$. Using two subarrays in our design allows us to have separate control of image displacement in Function 1 and Function 2. A larger Λ reduces the separation between the LCP and RCP field and hence forms finer edges on the detector. In our simulation, we used a $4f$ system with a focal length of 10 cm and 5 cm. In Fig. 4, the Λ for an edge resolution of 50 μm in Function 1, as shown in Fig. 4(c), is 1150 μm. Without loss of generality, the Λ for edge resolution of 90 μm in Function 2, as shown in Fig. 4(d), is 916.7 μm.

To conclude, we demonstrate numerically a VNIR dual band switchable edge imaging system achieved by MTF modulation with a Sb_2S_3 metasurface. Two Sb_2S_3 nanoblock arrays are interleaved on the same substrate. Each produces a separate phase profile, which is optimized and only becomes active for one wave band in one of the Sb_2S_3 states. Dynamic phase-change-induced tunability of the metasurface is therefore achieved via switching the Sb_2S_3 phase. The passive solid state, ultra-thin, post-fabrication tunable optical metasurface made of a phase change material given in this work provides a convenient platform for the implementation of subminiature hyperspectral optical imaging systems.

Funding. Gordon and Betty Moore Foundation; National Science Foundation (ECCS-1907423).

Disclosures. The authors declare no conflicts of interest.

Data availability. Data underlying the results presented in this paper are not publicly available at this time but may be obtained from the authors upon reasonable request.

Supplemental document. See Supplement 1 for supporting content.

REFERENCES

1. A. Daniels, *Field Guide to Infrared Systems, Detectors, and FPAs*, 2nd ed. (SPIE, 2010), Vol. FG15.
2. S. E. Umbaugh, *Digital Image Processing and Analysis: Human and Computer Vision Applications with CVIPtools* (CRC Press, 2010).
3. S. He, J. Zhou, S. Chen, W. Shu, H. Luo, and S. Wen, APL Photonics **5**, 036105 (2020).
4. D. Xu, S. He, J. Zhou, S. Chen, S. Wen, and H. Luo, Opt. Lett. **45**, 6867 (2020).
5. D. Xu, S. He, J. Zhou, S. Chen, S. Wen, and H. Luo, Appl. Phys. Lett. **116**, 211103 (2020).
6. S. He, J. Zhou, S. Chen, W. Shu, H. Luo, and S. Wen, Opt. Lett. **45**, 877 (2020).
7. J. W. Goodman, *Introduction to Fourier Optics* (Roberts and Company Publishers, 2005).

8. T. Li, X. Li, S. Yan, X. Xu, S. Wang, B. Yao, Z. Wang, and S. Zhu, Phys. Rev. Appl. **15**, 014059 (2021).
9. P. Genevet, F. Capasso, F. Aieta, M. Khorasaninejad, and R. Devlin, Optica **4**, 139 (2017).
10. A. Arbabi, Y. Horie, A. J. Ball, M. Bagheri, and A. Faraon, Nat. Commun. **6**, 7069 (2015).
11. N. Yu, P. Genevet, M. A. Kats, F. Aieta, J.-P. Tetienne, F. Capasso, and Z. Gaburro, Science **334**, 333 (2011).
12. T. Li, X. Xu, B. Fu, S. Wang, B. Li, Z. Wang, and S. Zhu, Photonics Res. **9**, 1062 (2021).
13. S. Zhang, P. Huo, W. Zhu, C. Zhang, P. Chen, M. Liu, L. Chen, H. J. Lezec, A. Agrawal, Y. Lu, and T. Xu, Laser Photonics Rev. **14**, 2000062 (2020).
14. J. Zhou, H. Qian, C.-F. Chen, J. Zhao, G. Li, Q. Wu, H. Luo, S. Wen, and Z. Liu, Proc. Natl. Acad. Sci. U.S.A. **116**, 11137 (2019).
15. S. Abdollahramezani, O. Hemmatyar, and A. Adibi, Nanophotonics **9**, 4075 (2020).
16. J. Zhou, H. Qian, J. Zhao, M. Tang, Q. Wu, M. Lei, H. Luo, S. Wen, S. Chen, and Z. Liu, Nat. Sci. Rev. **8**, nwaa176 (2021).
17. Y. Zhou, H. Zheng, I. I. Kravchenko, and J. Valentine, Nat. Photonics **14**, 316 (2020).
18. H. Kwon, D. Sounas, A. Cordaro, A. Polman, and A. Alù, Phys. Rev. Lett. **121**, 173004 (2018).
19. Y. Zhou, W. Wu, R. Chen, W. Chen, R. Chen, and Y. Ma, Adv. Opt. Mater. **8**, 1901523 (2020).
20. T. Zhu, C. Guo, J. Huang, H. Wang, M. Orenstein, Z. Ruan, and S. Fan, Nat. Commun. **12**, 680 (2021).
21. P. Huo, C. Zhang, W. Zhu, M. Liu, S. Zhang, S. Zhang, L. Chen, H. J. Lezec, A. Agrawal, Y. Lu, and T. Xu, Nano Lett. **20**, 2791 (2020).
22. S. M. Kamali, E. Arbabi, A. Arbabi, and A. Faraon, Nanophotonics **7**, 1041 (2018).
23. J. Zhou, H. Qian, G. Hu, H. Luo, S. Wen, and Z. Liu, ACS Nano **12**, 82 (2018).
24. M. Khorasaninejad, W. T. Chen, R. C. Devlin, J. Oh, A. Y. Zhu, and F. Capasso, Science **352**, 1190 (2016).
25. G. Sun, S. Peng, X. Zhang, and Y. Zhu, Nanomaterials **10**, 1064 (2020).
26. Z. Shi, M. Khorasaninejad, Y.-W. Huang, C. Roques-Carmes, A. Y. Zhu, W. T. Chen, V. Sanjeev, Z.-W. Ding, M. Tamagnone, K. Chaudhary, R. C. Devlin, C.-W. Qiu, and F. Capasso, Nano Lett. **18**, 2420 (2018).
27. B. Fu, T. Li, X. Zou, J. Ren, Q. Yuan, S. Wang, X. Cao, Z. Wang, and S. Zhu, J. Phys. D: Appl. Phys. **55**, 255105 (2022).
28. G. Yoon, J. Kim, J. Mun, D. Lee, K. T. Nam, and J. Rho, Commun. Phys. **2**, 129 (2019).
29. A. Howes, W. Wang, I. Kravchenko, and J. Valentine, Optica **5**, 787 (2018).
30. P. P. Iyer, M. Pendharkar, C. J. Palmstrøm, and J. A. Schuller, Nat. Commun. **8**, 1 (2017).
31. E. Arbabi, A. Arbabi, S. M. Kamali, Y. Horie, M. Faraji-Dana, and A. Faraon, Nat. Commun. **9**, 812 (2018).
32. M. Decker, C. Kremers, A. Minovich, I. Staude, A. E. Miroshnichenko, D. Chigrin, D. N. Neshev, C. Jagadish, and Y. S. Kivshar, Opt. Express **21**, 8879 (2013).
33. E. Feigenbaum, K. Diest, and H. A. Atwater, Nano Lett. **10**, 2111 (2010).
34. J. Zhou, H. Qian, C.-F. Chen, L. Chen, and Z. Liu, Nano Lett. **21**, 330 (2021).
35. M. Y. Shalaginov, S. D. Campbell, S. An, Y. Zhang, C. Ríos, E. B. Whiting, Y. Wu, L. Kang, B. Zheng, C. Fowler, H. Zhang, D. H. Werner, J. Hu, and T. Gu, Nanophotonics **9**, 3505 (2020).
36. M. N. Julian, C. Williams, S. Borg, S. Bartram, and H. J. Kim, Optica **7**, 746 (2020).
37. X. Shi, C. Chen, S. Liu, and G. Li, Results Phys. **22**, 103897 (2021).
38. K. V. Sreekanth, Q. Ouyang, S. Sreejith, S. Zeng, W. Lishu, E. Ilker, W. Dong, M. ElKabbash, Y. Ting, C. T. Lim, M. Hinczewski, G. Strangi, K.-T. Yong, R. E. Simpson, and R. Singh, Adv. Opt. Mater. **7**, 1900081 (2019).
39. C. Ríos, Q. Du, Y. Zhang, C.-C. Popescu, M. Y. Shalaginov, P. Miller, C. Roberts, M. Kang, K. A. Richardson, T. Gu, S. A. Vitale, and J. Hu, "Ultra-compact nonvolatile photonics based on electrically reprogrammable transparent phase change materials," arXiv:2105.06010, (2021).
40. M. Delaney, I. Zeimpekis, D. Lawson, D. W. Hewak, and O. L. Muskens, Adv. Funct. Mater. **30**, 2002447 (2020).
41. W. Dong, H. Liu, J. K. Behera, L. Lu, R. J. H. Ng, K. V. Sreekanth, X. Zhou, J. K. W. Yang, and R. E. Simpson, Adv. Funct. Mater. **29**, 1806181 (2019).
42. S. AbdollahRamezani, K. Arik, A. Khavasi, and Z. Kavehvash, Opt. Lett. **40**, 5239 (2015).
43. H. Yang, Z. Xie, H. He, Q. Zhang, J. Li, Y. Zhang, and X. Yuan, Opt. Lett. **46**, 3741 (2021).
44. W. Jia, R. Menon, and B. Sensale-Rodriguez, Opt. Express **30**, 6808 (2022).
45. M. A. Kats, P. Genevet, G. Aoust, N. Yu, R. Blanchard, F. Aieta, Z. Gaburro, and F. Capasso, Proc. Natl. Acad. Sci. U.S.A. **109**, 12364 (2012).
46. Z. e. Bomzon, G. Biener, V. Kleiner, and E. Hasman, Opt. Lett. **27**, 1141 (2002).
47. M. Khorasaninejad and K. B. Crozier, Nat. Commun. **5**, 5386 (2014).
48. B. H. Chen, P. C. Wu, V.-C. Su, Y.-C. Lai, C. H. Chu, I. C. Lee, J.-W. Chen, Y. H. Chen, Y.-C. Lan, C.-H. Kuan, and D. P. Tsai, Nano Lett. **17**, 6345 (2017).